NUMERICAL INVESTIGATION OF PROPELLER STALL FLUTTER

Murray McKechnie
University of Glasgow
Glasgow, United Kingdom

George N. Barakos
University of Glasgow
Glasgow, United Kingdom

ABSTRACT

Aeroelastic analyses are part of design of modern propeller blades. Most of the times advanced numerical simulations are used, involving computational fluid dynamics. However, the coupling between fluid and structure is usually missing. In this paper we utilise two fluid structure interaction methods namely: a modal time-marching and a quasi-static approach. An in house method is used and different propeller designs were tested. A limited number of experiments is available and this was alleviated using new experiments as part of the Numerical and Experimental Study of Propeller Aeroelasticity (NESPA) project. Beam and 3D finite element models were used to represent the structure and time-marching and quasi-steady results were compared. It was found that regardless of the small differences in the aerodynamic loads between time-marching and quasi-static computations, the final blade deformations were comparable. Comparisons of the required power showed little differences between rigid and aeroelastic calculations. Looking at the detailed strain fields for the aeroelastic cases similar trends were observed between physical experiments and numerical simulations.

NOTATION

*

Symbols

α Modal amplitude

ζ Structural Damping

τ Pseudo Time Step

ϕ Deformed Shape

ω Eigen-pulsation

$\mathbf{f}$ Structural Forcing Term

R Residual Vector

S Source Term

t Real Time Step

W Vector of Conserved Variables

*

Acronyms

ERF European Rotorcraft Forum

VFS Vertical Flight Society

ADT Alternating Digital Tree

BILU Block Incomplete Lower-Upper

CFD Computational Fluid Dynamics

CSD Computational Structural Dynamics

FE Finite Element

FEM Finite Element Method

HMB3 Helicopter Multi Block 3

IDW Inverse Distance Weighting

MLS Moving Least Squares

MUSCL Monotone Upstream-centred Scheme for Conservation Laws

SAS Scale Adaptive Simulation

SST Shear Stress Transport

INTRODUCTION

Stall flutter is defined as the oscillation of a body due to the partial or full separation of the flowfield around it (Ref. 1). Propeller blades have operating conditions within the flight envelop that can lead to stall. Where the blade have high rotational rates with low axial velocity, i.e. low advance ratio, where $J = \frac{V}{nD}$. Here, V is the axial velocity, n is the rotational frequency and D is the diameter. These stall characteristics are obviously also dependant on the blade pitch angle. These conditions can occur on the runway at take-off or they may appear in new eVTOL aircraft in the transition stages from hover to forward flight. There is also a constant demand for better performing, quieter blades which often means thinner blade sections. Also, design characteristics such as larger twist, swept tip sections and tip anhedral can make the blades more susceptible to stall. Following on from work by Higgins (Ref. 2), where it was shown that stall flutter is driven by the design but the non-linear, stalled aerodynamics, means that the flutter boundary of stall flutter is significantly reduced in comparison with bending-torsion flutter. Work is now being undertaken at the University of Glasgow to further investigate this phenomena both experimentally and numerically. There is a serious lack of experimental stall flutter studies and often cases where data exists, these were accidental occurrences during performance testing which led to the test runs being shut down. (Ref. 3). In recent years, experimental tests for the MENtOR propeller blade have been conducted on the UK National Rotor Rig (Ref. 4). These campaigns have also considered the onset of stall on these blades (Ref. 5). This works looks at early comparisons between numerical and experimental data and numerical static and dynamic aeroelastics.

METHODOLOGY

CFD Solver

In this work the CFD solver HMB3 is employed. This solver has a long, well accredited history primarily associated to rotorcraft flight. The original work was primarily helicopter based flight (Refs. 7, 8). However, in terms of this work there has also been a significant history with propeller cases. These cases have been conducted for validation in both installed and isolated flight conditions (Refs. 16, 17). There has also been validation cases with well recognised propeller experimental campaigns such as the that of the JORP blade (Ref. 18), and the IMPACTA tests (Refs. 19,20). There has also been experimental inflow investigations at the University of Glasgow with a model propeller blade in axial flight and at yaw (Ref. 21).

In HMB3 the Navier-Stokes equations applied to a cell-centred, finite volume approach on a multi-block grid. The standard RANS/URANS system of ordinary differential equations are shown in equations 1-2.

$$\frac{dW}{dt} + R(W) = S \text{ Steady} \tag{1}$$

$$\frac{dW}{dt} + \frac{dW}{d\tau} + R(W) = 0 \text{ Unsteady} \tag{2}$$

where, W is the vector of conserved variables, R is the residual vector, S is the source term, t is the real time step and τ is the pseudo time step.

For all methods in HMB3 the convective fluxes are evaluated with the Osher (Ref. 9) approximate Riemann solver. We discretize the viscous terms with second order central differences in space. In order to provide high order accuracy in space the Monotone Upstream-centred Scheme for Conservation Laws (MUSCL) with developments by Leer (Ref. 10)are employed.

For the steady-state flow calculations, the flow is calculated in a non-inertial reference frame. Therefore, a source term and mesh velocities are used to account for the centripetal and Coriolis accelerations. For the unsteady time-marching method, the temporal integration is performed with the implicit dual-time stepping technique of Jameson (Ref. 12). For each time step there is a pseudo-time τ where the solution is marched to steady state. The linearised system is then solved with the Generalised Conjugate Gradient method with a Block Incomplete Lower-Upper (BILU) factorisation (Ref. 13).

Fluid Structure Interaction

Static Aeroelasticity An in house computer code coined 'Middleware' is used. Middleware is a communications utility within the HMB3 tool-set. It makes it easier to provide the required data format between our CFD solver and the structural solver (NASTRAN). It forms a link which takes a CFD flow solution, passes forces and moments to the structural model and then converts the deformed structure back onto the CFD mesh. This is an iterative process between fluid and structure until the deformation converges. This loose-coupling means that it is applicable for attached flow cases with steady flow solutions. However, it cannot be used for stalled cases as it will not show a true dynamic interaction between fluid and structure.

The Middleware process is demonstrated in Figure 1. The converged flow solution for a rigid structure and its surface mesh are passed to Middleware. The flow solution is used to calculate the aerodynamic loads according to the structural model, e.g., the required NASTRAN force input will vary depending on if a beam or full-fem model is to be used. When this file is generated NASTRAN is started and the deformation is calculated, for rotary blade the centrifugal effects are accounted for in the structural model. This is done using the NASTRAN RFORCE commands. After the structural deformation is calculated Middleware post-processes the deformation and interpolates the deformation onto the CFD surface mesh. A set of grid points are generated that are situated on the surface of the blade and are representative of the aerodynamic surface, these points have a similar resolution to that of the FEM mesh. These points are then defined as a set and are connected to the nearest FEM mesh grid point with a rigid bar. We do this because it makes it easier to have a well defined set of points that represent the deformed surface and can be used for the interpolation of the mesh deformation. The purpose of the rigid bar is that when the FEM mesh deforms then these points will also translate and rotate to represent the deformed structural shape. Middleware then passes this deformed surface mesh back to HMB3 where the deformed volume mesh is calculated and the CFD simulation continues with the now deformed mesh. This deformation causes a change in the aerodynamic loads which is why it is an iterative process between fluid and structure through Middleware.

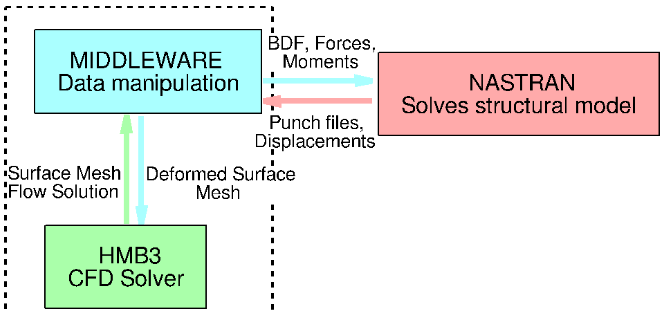

Figure 1. Schematic of HMB3/NASTRAN interface.

The mesh deformation procedure is the same for both the static aeroelastic method (middleware) and the dynamic aeroelastic method (modal method).

Dynamic Aeroelasticity The dynamic aeroelasticity method of HMB3 is based on the modal method (Ref. 6), in our cases we use it to target our stalled flow cases with dynamic fluid-structure interaction. However, it could also be used for attached flow cases. The reason that we do not do this is that it is configured in HMB3 to operate with an unsteady flow solution and therefore it would require unnecessary expense over our middleware method. The modal method is a coupled method between fluid and structure, it uses eigenmodes which are input from a structural modal solution and projects the forces to the mode shapes, from this the deformation can be solved as a function of the structures eigenmodes. Like middleware, the mesh deformation procedure is based on the inverse distance weighting interpolation.

The same finite element model that is used for the middleware, attached flow cases is also used here. Here the NASTRAN model is used to obtain the structural mode shapes and frequencies. The structural model itself is a full finite element model (FEM), it has glue connection between each of the parts and the material properties are supplied to each part. Due to the requirement for glue connections, eigenmode result requirements and structural solver limitations, an implicit nonlinear method is used.

The structural model uses the implicit nonlinear NASTRAN solver (SOL 400). This solver is used to solve for the eigenmodes, it also allows loads to be applied. In our case it is the centrifugal load and including this in the eigenmode calculation accounts for rotational stiffening. This solver is also required in order to obtain these mode shapes with applied load and apply glue connections between parts. It is essential that the unit system here directly matches that of the CFD simulation. This is because the mode shapes are mass scaled. This means that the generalized mass of the model is calculated then each displacement vector is scaled by dividing through by the generalised mass. The representative length of each of these vectors is crucial to ensure the modal force calculation is correct. Hence why the unit system must be matched with the force terms in the combined CFD-CSD calculation.

Before the CFD calculation begins the CFD solver takes the supplied mode shapes and interpolates each of the eigenmodes onto the CFD mesh. This is conducted using the MLS method. This means that the CSD to CFD mesh interpolation only needs to be conducted once at the start of the simulation and then the interpolated eigenmode deformed shapes for the CFD mesh can be used throughout the rest of the simulation for every time step. Also the transform for aerodynamic loads to structure can be applied directly to these deformed CFD mesh shapes rather than requiring further interpolation.

For each time step the deformed blade shape, ϕ is computed from the rigid blade shape and the modal amplitude coefficients, α_i, multiplied by the provided mode shapes, ϕ_i. To solve for the modal amplitudes Eq 4 is used. Where ζ_i is the applied structural damping, typically this starts around 0.4 for each calculation in order to stabilise the deformation, then reduced to 0.01 to observe the fluid-structure response, ω represents the frequency for each eigenmode and $\mathbf{f}$ is the force matrix. This comes from the projection of the forces on the blade on the mode shapes.

$$\phi = \phi_0 + \sum_{i=1}^{n_m} \alpha_i \phi_i \tag{3}$$

$$\frac{\partial^2 \alpha_i}{\partial t^2} + 2\zeta_i \omega_i \frac{\partial \alpha_i}{\partial t} + \omega_i^2 \alpha_i = \mathbf{f} \cdot \phi_i \tag{4}$$

Grid Deformation The grid deformation is performed in HMB3, firstly there is an interpolation between the calculated deformed surface and the surface mesh. This is done using the Moving Least Square (MLS) method. There is also the option to have a parent and child approach, if you consider an installed propeller on a wing. The blade deformation (child) can be calculated and then displaced with a wing deformation (parent). However, for these cases this is not required. To complete the volume mesh the Inverse Distance Weighting (IDW) is used. There are other mesh deformation methods used in HMB3, though these were not used in this work.

THE MENTOR PROPELLER BLADE

The MENtOR blade used for this project is of a similiar design to an eVTOL tiltrotor blade. It has three aerofoils, these are the NACA 64-128 at the root, the Vertol V23010_1.58 at 60%R and the Vertol V43015_2_48 at the blade tip. The twist and chord distribution can be seen in Figure 2. The blade is comprised of six main parts, these are: blade skin, tip cap, spar, rear filler, spar filler and the root fitting. The blade sections can be observed in Figure 3 and the material list in Table 1.

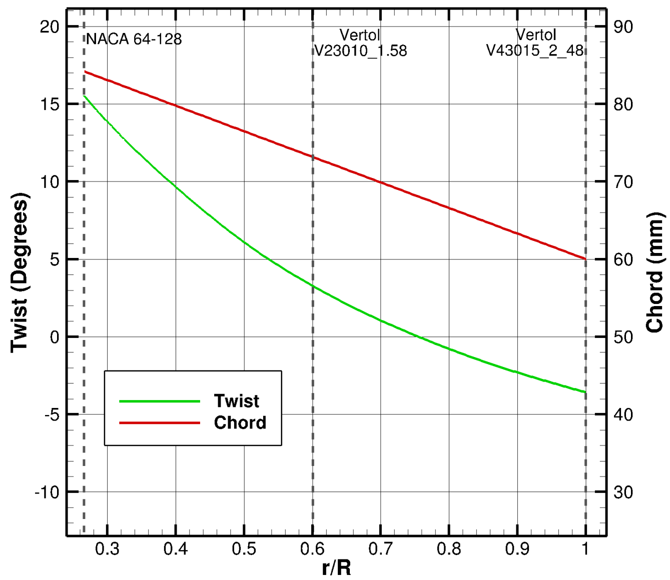

Figure 2. MENtOR propeller blade, sections, twist and chord.

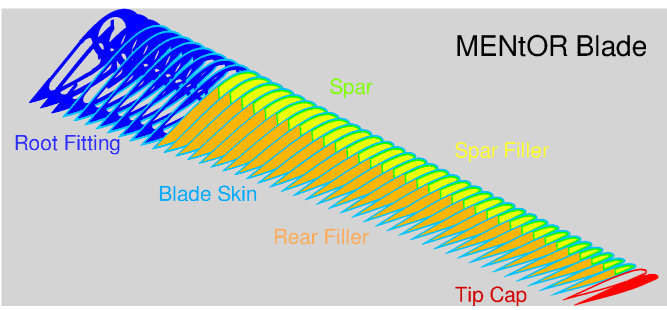

Figure 3. MENtOR blade parts.

CFD MESH

Chimera, body fitted structured, multi-block grids were used here. The background and blade domain, can be seen in Figures 4 and 5, respectively. The background mesh has 11.5M cells and the blade mesh has 6.6M cells, therefore 18.1M cells overall. For the blade mesh, the chimera boundary is 0.5 chord lengths off of the surface with a wall distance of $10^{-}5$ root chords and a hyperbolic distribution law. There is a centre-body in the background mesh which is a perfect cylinder which runs the entire length of the domain and has a radius of 0.5 root chords. The inflow and outflow boundaries have far-field conditions, see Figure 4).

Table 1. MENtOR Blade, parts and materials.

Part	Material
Skin	Carbon Fibre, [(0/90)/(+45/-45)/(+45/-45)/(0/90)]
Tip Cap	Carbon Fibre, [(0/90)/(+45/-45)/(+45/-45)/(0/90)]
Spar	Carbon Fibre, [(0/90)/(0/90)/(0/90)/(0/90)]
Rear Filler	ROHACELL®71HERO
Spar Filler	ROHACELL®71HERO
Root Fitting	AA7075-T651

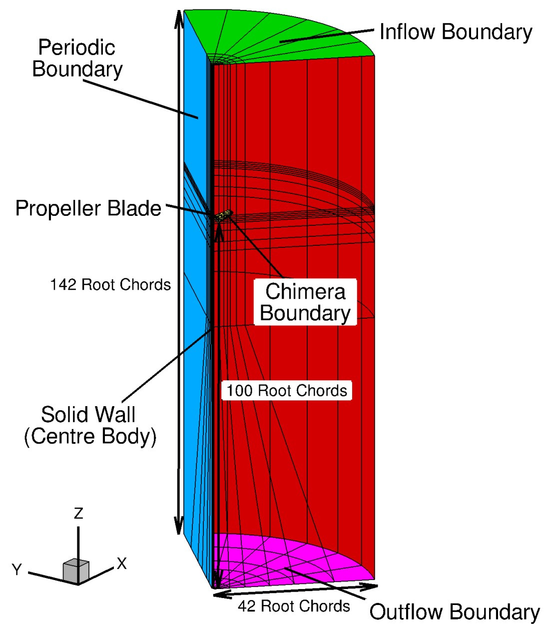

Figure 4. MENtOR background CFD mesh.

FINITE ELEMENT MODELS

The finite element model consists of 1.9M tetrahedral elements. For static aeroelastic analyses, the linear static SOL101 is used. The aerodynamic loads are precomputed and formatted for NASTRAN. The centrifugal term is also applied using the NASTRAN RFORCE command. For dynamic aeroelastic analyses the implicit nonlinear SOL400 method is used. This allows for an eigenmode analysis using "glue" connections between mesh parts.

A physical tap test using free-free conditions was conducted by the BLADE lab at the University of Bristol and this was replicated numerically. The frequency comparison can be seen in Table 2, and the mode shape comparison can be found in Figure 9. This comparison was used to validate the model, before simulating the blades on the propeller rig. The use of the centrifugal term in the eigenmode analysis accounts for the centrifugal stiffening for the combined CFD/CSD simulation.

RESULTS AND DISCUSSION

Static Aeroelasticity

Cases were computed with steady flow assumptions and the blade torque was compared with wind tunnel data. These are presented in Figures 10 and 11, for pitch angles, 16, 25.5 and 35.7 degrees at the 75% radial section, 1080 revolutions per

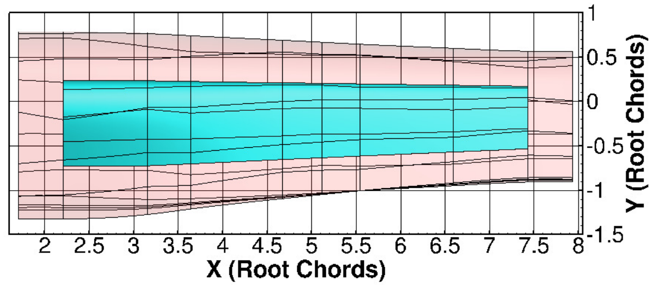

(a) Propeller blade domain, XY plane.

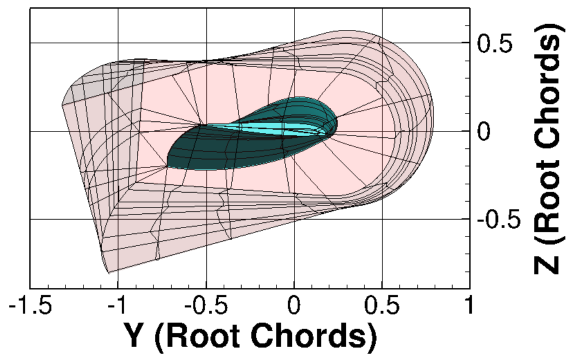

(b) Propeller blade domain, YZ plane.

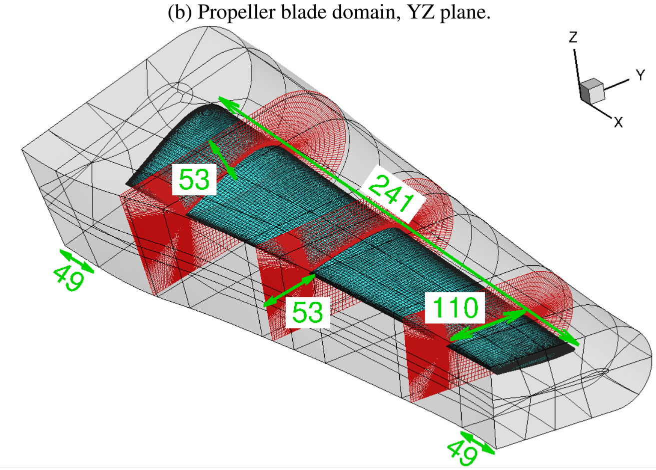

(c) Propeller blade mesh.

Figure 5. MENtOR blade, CFD mesh.

minute, with advance ratios from 0.08 to 1.3. The advance ratios were restricted by what was achievable in the wind tunnel, between power limits and reverse blade thrust. Figure 10 displays the numerical thrust and torque compared to experimental values. It can be observed that the simulation resolved the torque quite well. The comparisons suffer at the lower advance ratio and high collective, due to the steady periodic flow assumptions used for this analysis. What can be observed is that the numerical torque is slightly less than the experimental torque for all advance ratios. However, this is expected due to the numerical simulation only containing the blade with no spinner or rig present.

The displacements that are induced from these forces are presented in Figure 11. As expected the tip quarter chord deformation plot follows the same trend as the loads. However, the lower advance ratio, stalled cases, suffered with the the steady flow assumption and require unsteady modelling. The results also shown how stiff the blades are, with the maximum recorded displacement approaching 2.4mm, and the maximum change in pitch angle at the tip reaching -0.025 degrees. Here, negative results indicate pitch down deformations.

Table 2. Free-free structural frequency comparisons and numerical, fixed root, modal frequencies.

Mode	Experimental Frequency (Hz)	NASTRAN Free-Free (Hz)	NASTRAN Fixed Root, 3000 RPM (Hz)
1	257.7-261.3	261.3	149.3
2	733.6-743.2	750.9	421.8
3	916.3-934.4	1055.9	567.8
4	1270.0-1301.9	1319.0	1118.0
5	1397.1-1412.4	1421.6	1413.7
6	-	2015.5	1761.9
7	-	2073.8	2014.9
8	-	2452.4	2414.5
9	-	2682.4	2519.2
10	-	2904.6	2728.3

Dynamic Aeroelasticity

Due to the limitations of the steady flow assumptions the modal method was then used. These cases are for the advance ratio of 0.3, 3000 revolutions per minute and the pitch angles of 32 and 35.6 degrees at the 75% radial section. The flow around the blades can be appreciated from Figure 12.

The modal amplitudes can be observed in Figure 13, the largest are for the first mode which is the first bending mode. The mode shape supplied bends down hence why the output amplitude is negative, this is the main contribution towards aeroelastic coning of the blade. Due to the stalled nature of these flows the amplitudes are aperiodic for all modes. However, it can be observed that the fluctuations are larger in the 35.6 degree case which is more stalled. The higher order modes were found to have a very small contribution on the computed deformed shape.

The modal forces are shown in Figure 14. Again, each mode is aperiodic and the magnitudes and oscillations of the forces are slightly larger for the 35.6 degree case. Figure 15 displays the detailed view of the main torsional modes for both pitch angles. The magnitudes of oscillations are larger for the 35.6 degree, more stalled case. There is also some frequency beating, particularly in the 5^{th} mode.

Frequency domain plots were obtained using a Hanning windowing method, and zero damping was applied before the fourier transform was computed. The returned spectra plots can be found in Figure 16 for the modal amplitudes, and 17 for the forces. The black dashed lines indicate the blade passing frequency and its harmonics, the orange dashed lines indicate the structural mode and its harmonics. For attached flows, the peaks would only occur on the blade passing frequency, the structural modes and the harmonics. In these highly stalled

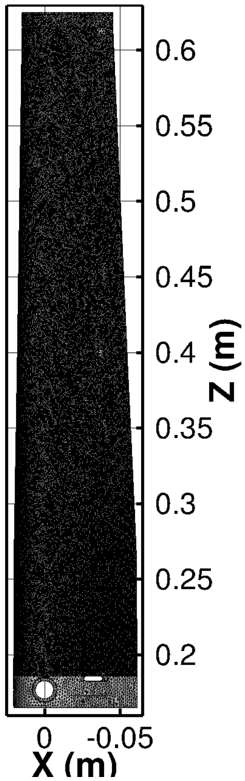

Figure 6. Overall view of the FE mesh.

cases there are additional peaks attributed to the stalled flow. The broadband content in the signals is also indicative of the stall in these flows. However, as expected, the largest amplitudes occur at the structural modal frequencies.

Figure 18 displays the deformations for the blade tip, as absolute quarter-chord point displacements and as changes in the local pitch angle. The quarter-chord is displaced about 7mm and 7.3mm for the 32 and 35.6 degree cases respectively. The minimum to maximum deviations are around $1mm$ for both cases. The local changes in pitch angle plot displays that the propeller deforms dynamically at very high frequencies but at small magnitudes of 0.05 degrees on average. This small change in pitch angle are not enough for the blade to diverge, and keep the oscillations bounded.

CONCLUSIONS

In this work static and dynamic aeroelastic analyses of the MENtOR Propeller blade were conducted using the HMB3 software. The propeller torque was shown to match very well with the experiments other than where the low advance ratio cases where the employed steady flow assumptions suffer. The dynamic calculations show significant non-harmonic content in both modal amplitudes and forces. Even if the deformations were small, these were torsional and bending deformations that increased as the flow stall progressed. The non-harmonic content suggests that the flow is driving the oscillation in the structure indicating flutter onset before divergence. This investigation continues with different flow cases aiming to establish the onset of flutter across the operating range of the blades.

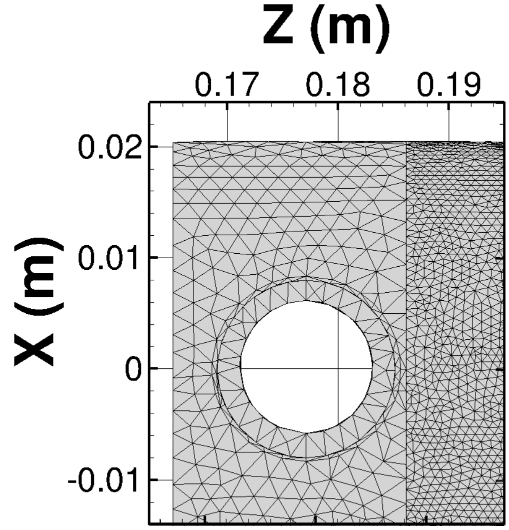

Figure 7. Detailed FE mesh view at the blade pin attachment.

Author contact:
Murray McKechnie, m.mckechnie.1@research.gla.ac.uk, George N. Barakos, george.barakos@glasgow.ac.uk.

ACKNOWLEDGMENTS

The support of DOWTY Propellers via the NESPA project is gratefully appreciated.

REFERENCES

1. Fung, Y.C., “An Introduction to the Theory of Aeroelasticity”, *Dover Publications*, 3rd Edition, 1993.

2. Higgins, R., “Investigation of Propeller Stall Flutter”, *Ph.D. thesis, University of Glasgow 2020*.

3. Higgins, R., Barakos, G., and Filippone, A., “A review of propeller stall flutter”, *he Aeronautical Journal*, Vol. 126, 2022, pp.1678-1717.

4. Zagaglia, D., Croke, A. D., Green, R. B., and Barakos, G. N., “Development of the UK National Rotor Rig For Aeroelastic Testing of Rotary Wings”, *49th European Rotorcraft Forum (ERF 2023)*, 2023.

5. Croke, A. D., Zagaglia, D., Woodgate, M. A., Green, R. B., and Barakos, G. N., “Experimental Investigation into the Onset of Stall Flutter on Tiltrotor Blades”, *49th European Rotorcraft Forum (ERF 2023)*, 2023.

6. Babu, S.V. and Loupy, G.J.M. and Dehaeze, F. and Barakos, G.N. and Taylor, N.J., “Aeroelastic simulations of stores in weapon bays using Detached-Eddy Simulation”, *Journal of Fluids and Structures*, Vol. 66, October 2016, pp. 207–228.

7. R. Steijl and G. N. Barakos and K. Badcock, “A framework for CFD analysis of helicopter rotors in hover

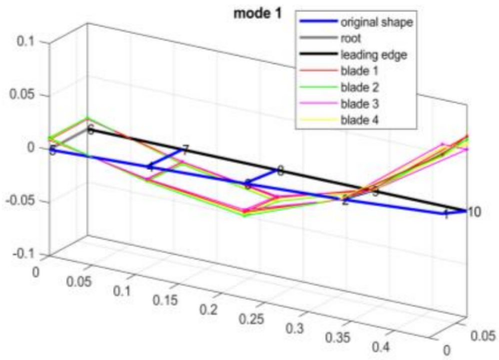

(a) Bristol BLADE Lab Mode 1

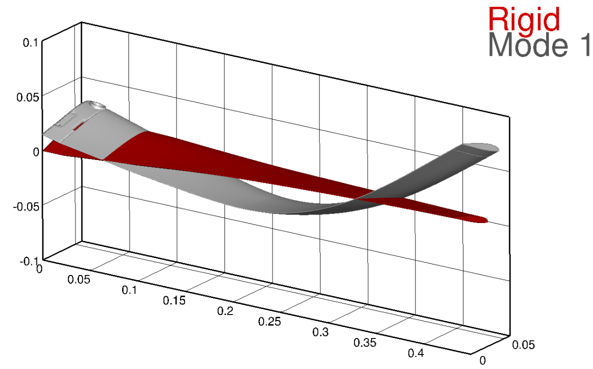

(b) FEM Eigen-Analysis Mode 1

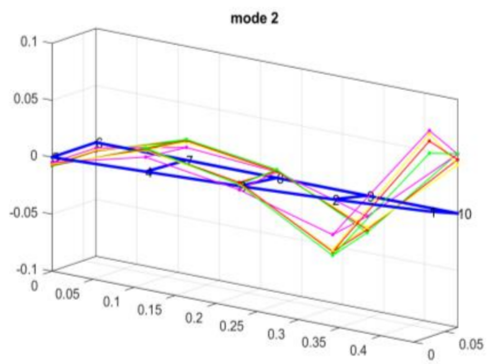

(a) Bristol BLADE Lab Mode 2

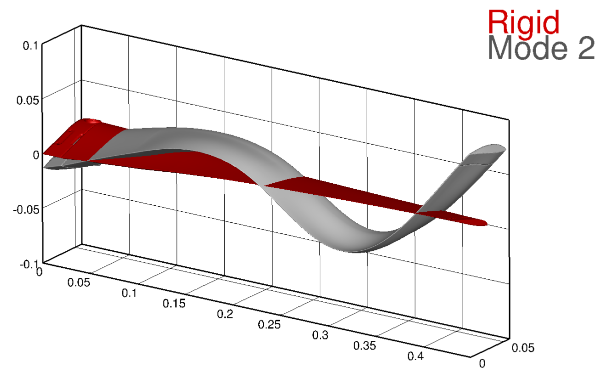

(b) FEM Eigen-Analysis Mode 2

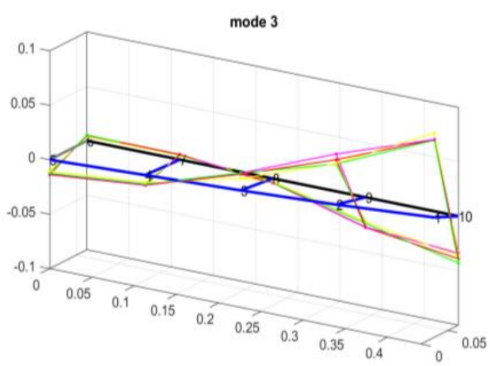

(a) Bristol BLADE Lab Mode 3

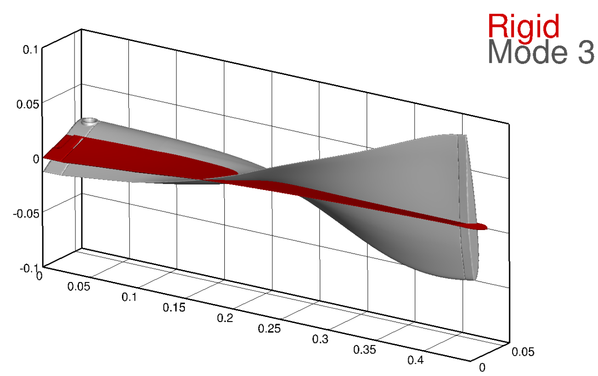

(b) FEM Eigen-Analysis Mode 3

Figure 8. Mode shape comparison between tap test and FEM eigen-analysis. Tests were conducted by Bristol University as part of the MENtOR project.

and forward flight", *International Journal for Numerical Methods in Fluids*, Vol. 51, 2006, pp. 819-847, DOI: 10.1002/d.1086.

8. R. Steijl and G. N. Barakos, "Sliding mesh algorithm for CFD analysis of helicopter rotor-fuselage aerodynamics", *International Journal for Numerical Methods in Fluids*, Vol. 58, 2008, pp. 527-549, DOI: 10.1002/d.1757.

9. S. Osher and S. Chakravarthy, "Upwind schemes and boundary conditions with applications to Euler equations in general geometries", *Journal of Computational Physics*, Vol. 50, 1983, pp.447-481, DOI: 10.1016/0021-9991(83)90106-7.

10. B. van Leer, "Towards the ultimate conservative difference scheme. V.A second-order sequel to Godunov's Method", *Journal of Computational Physics*, Vol. 32, 1979, pp. 101-136, DOI: 10.1016/0021-9991(79)90145-1.

11. G. D. van Albada and B. van Leer and W. W. Roberts, "A Comparative Study of Computational Methods in Cosmic Gas Dynamics", *Astronomy and Astrophysics*,

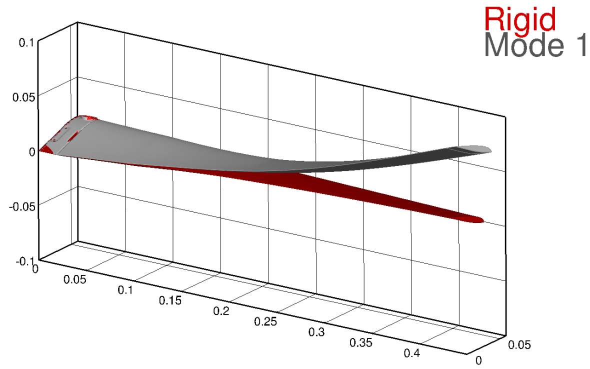

(a) Mode 1

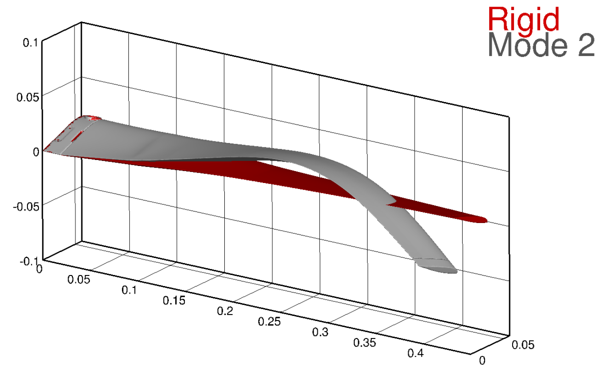

(b) Mode 2

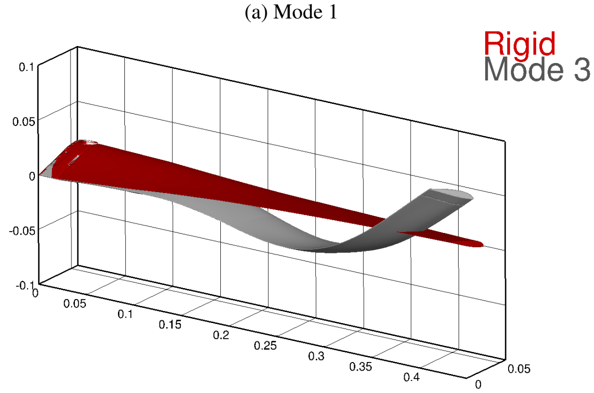

(c) Mode 3

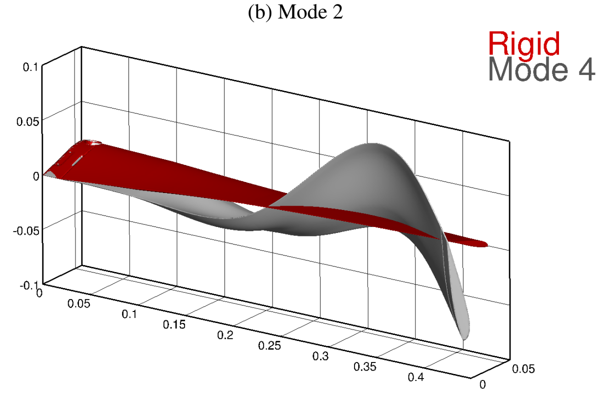

(d) Mode 4

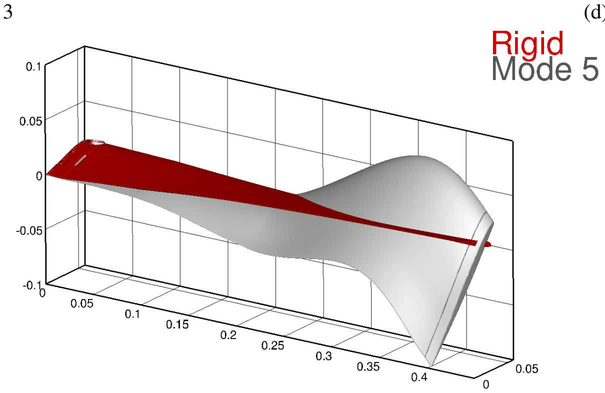

(e) Mode 5

Figure 9. Mode shapes of the MENtOR blade obtained at fixed-root conditions, rotating at 3000 RPM using NASTRAN.

Vol. 108, 1982, pp. 76-84, DOI: 10.1007/978-3-642-60543-7.

12. A. Jameson, "Time-Dependent Calculations Using Multigrid, with Applications to Unsteady Flows past Airfoils and Wings", *AIAA 10th Computational Fluid Dynamics Conference*, 1991.

13. O. Axelsson, "Iterative Solution Methods", *Cambridge University Press: Cambridge, MA*, 1994, DOI: 10.1017/CBO9780511624100.

14. MA. Woodgate and GN. Barakos, "An Implicit Hybrid Method for the Computation of Rotorcraft Aerodynamic Flows", *AIAA SciTech Forum, 54th Aerospace Sciences Meeting*, 2016, San Diego, California.

15. F. R. Menter, "Two-Equation Eddy-Viscosity Turbulence Models for Engineering Applications", *AIAA Journal*, Vol. 32, 1994, pp. 1598-1605, DOI: 10.2514/3.12149.

16. G. Barakos and C. Johnson, "Acoustic comparison of propellers", *International Journal of Aeroacoustics*, Vol. 15, 2016, pp. 575-594, DOI: 10.1177/1475472X16659214.

17. R.J. Higgins and A. Zarev and G.N. Barakos and R.B. Green, "Numerical Investigation of a Two-Bladed Propeller Inflow at Yaw", *Journal of Aircraft*, Vol. 57, 2020, DOI: 10.2514/1.C035647.

18. N. Scrase and M. Maina, "The Evaluation of Propeller Aero-acoustic Design Methods by Means of Scaled-Model Testing Employing Pressure Tapped Blades and Spinner", *International Council of the Aeronautical Sci-*

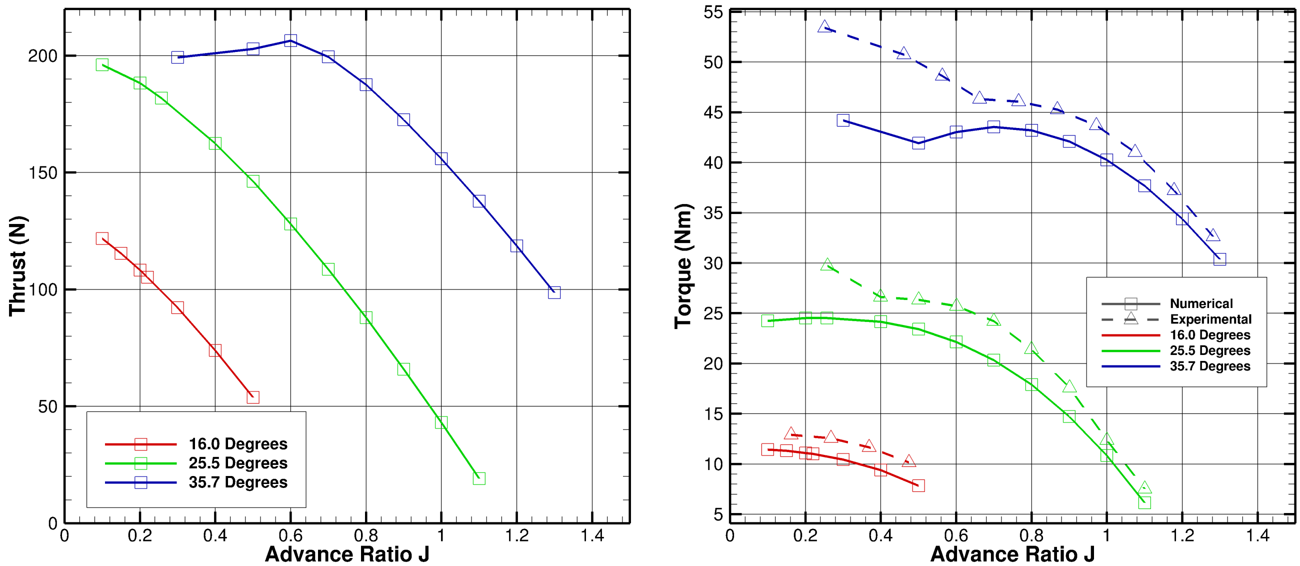

(a) Thrust.

(b) Torque.

Figure 10. Thrust obtained from simulations and comparison between estimated torque and recent wind tunnel experiments performed by Croke et al. (Ref. 5). MENtOR blade, 1080RPM, pitch angles of 16, 25.5 and 35.7 degrees.

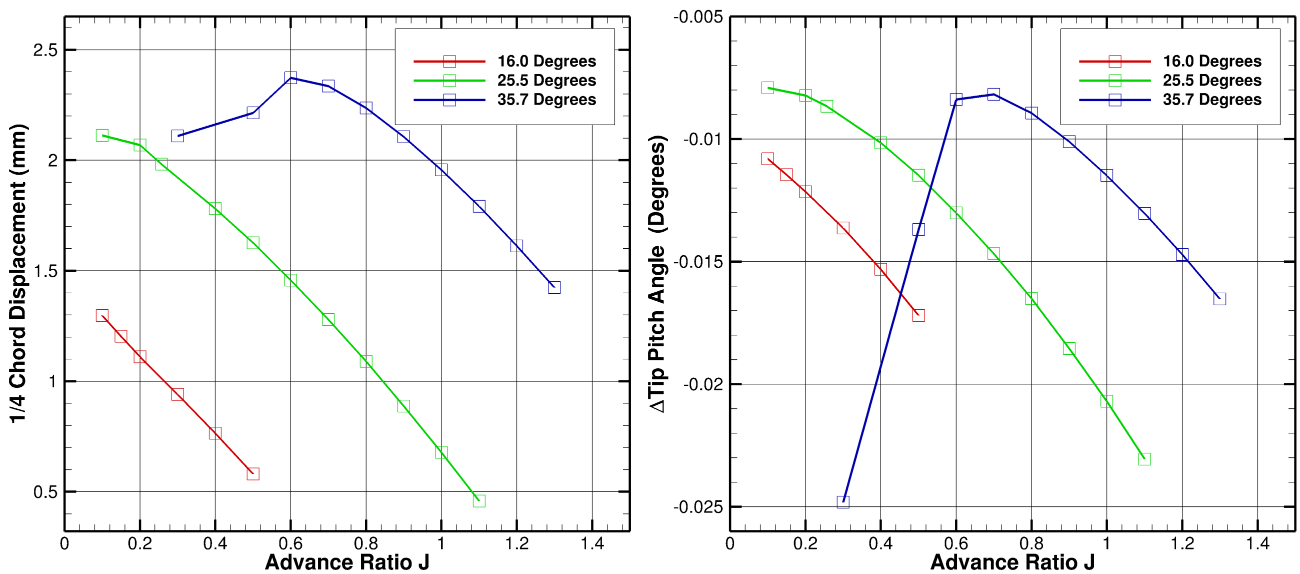

(a) Quarter chord tip displacement.

(b) Change in blade tip pitch angle from rigid to deformed.

Figure 11. Static aeroelastic tip displacements. MENtOR blade, 1080RPM, pitch angles of 16, 25.5 and 35.7 degrees.

ences, 19th ICAS Congress, Anaheim, California, USA, 1994, ISBN: 1563470845.

19. A. Gomariz-Sancha and M. Maina and A.J. Peace, "Analysis of propeller-airframe interaction effects through a combined numerical simulation and wind-tunnel testing approach", *53rd AIAA Aerospace Sciences Meeting*, Kissimmee, Florida, 2015, DOI: 10.2514/6.2015-1026.

20. A. Knepper and N. Bown, "IMPACTA Wind-tunnel Instrumentation Specification", *Dowty Propellers (GE Aviation Systems Ltd)*, 2014, ITS 01777, Issue 3.

21. A. Zarev and R.B. Green, "Experimental investigation of the effect of yaw angle on the inflow of a two-bladed propeller", *Aerospace Science and Technology*, Vol. 103, 2020, DOI: 10.1016/j.ast.2020.105940.

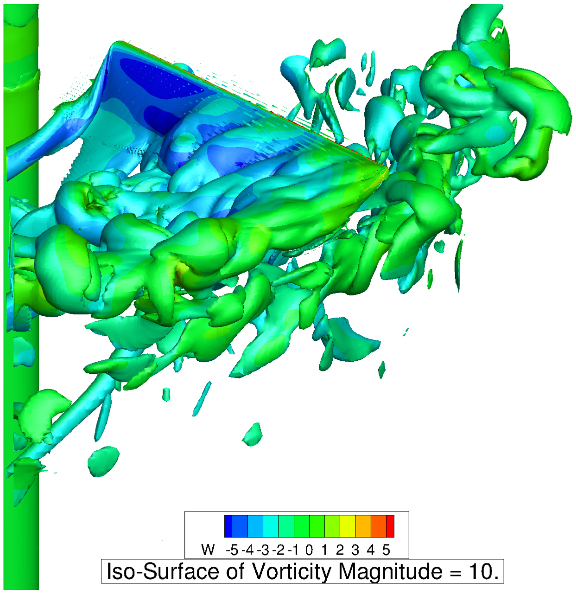

(b) 32 Degrees.

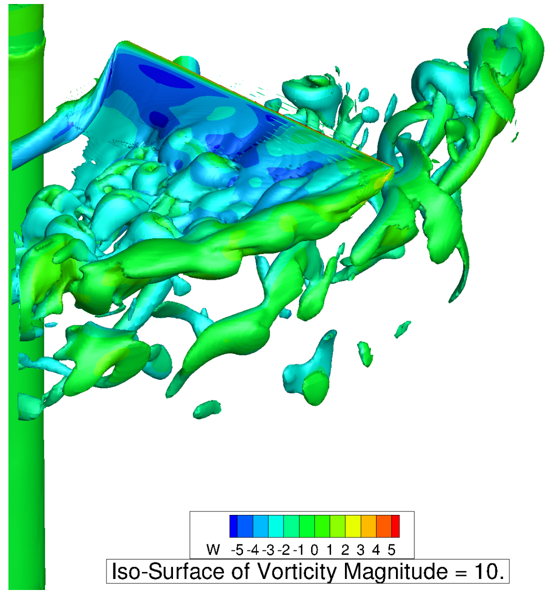

(c) 35.6 Degrees.

Figure 12. Instantaneous view of the flow around the MENtOR blade, 3000 RPM, advance ratio J=0.3, pitch angles of 32 and 35.6 degrees at 75%R, time-marching simulation.

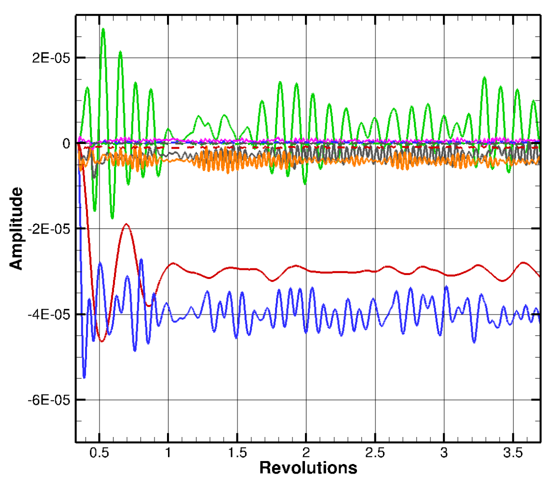

(b) 32 Degrees.

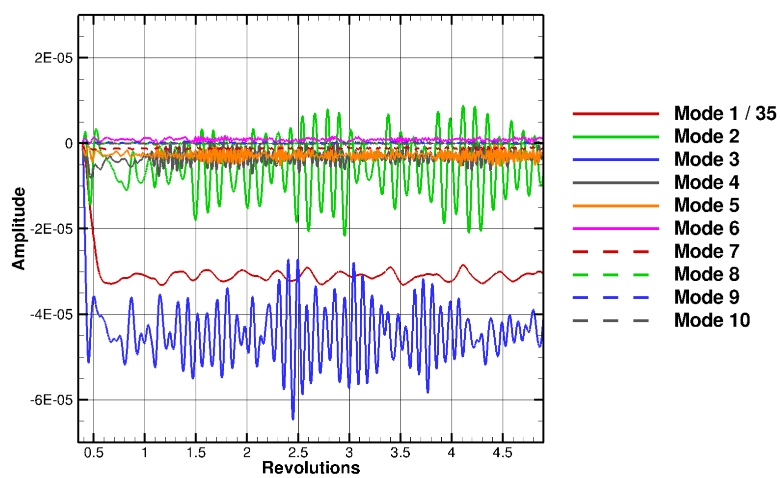

(c) 35.6 Degrees.

Figure 13. Time history of modal amplitudes. MENtOR blade, 3000 RPM, advance ratio J=0.3, pitch angles of 32 and 35.6 degrees at 75%R.

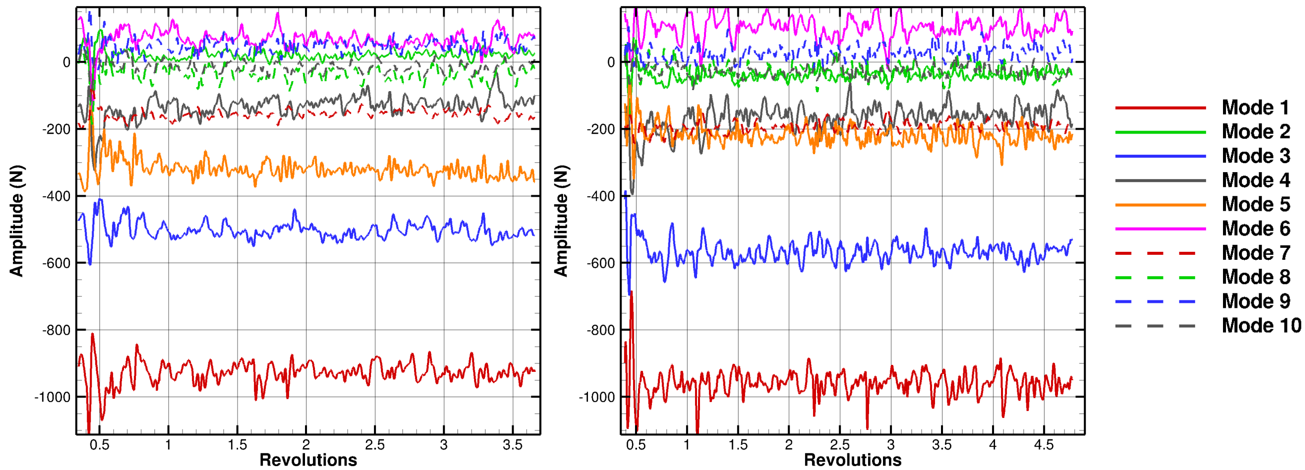

(b) 32 Degrees. (c) 35.6 Degrees.

Figure 14. Time history of modal forces. MENtOR blade, 3000 RPM, advance ratio J=0.3, pitch angles of 32 and 35.6 degrees at 75%R.

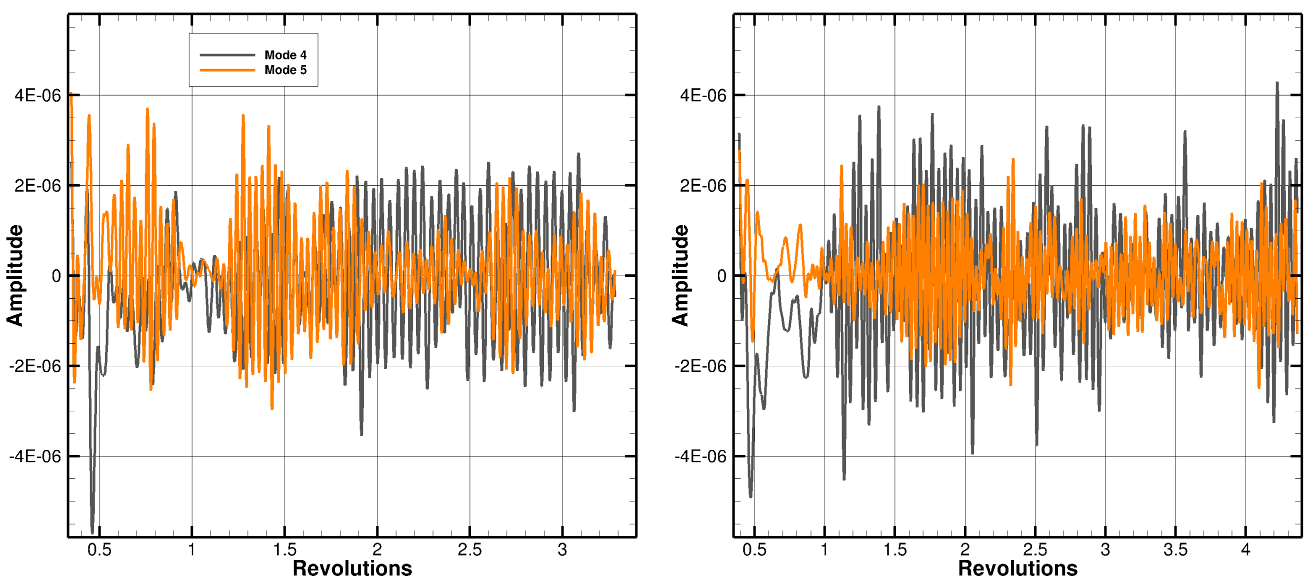

(b) 32 Degrees. (c) 35.6 Degrees.

Figure 15. Modal amplitudes, detailed view. MENtOR blade, 3000 RPM, advance ratio J=0.3, pitch angles of 32 and 35.6 degrees at 75%R.

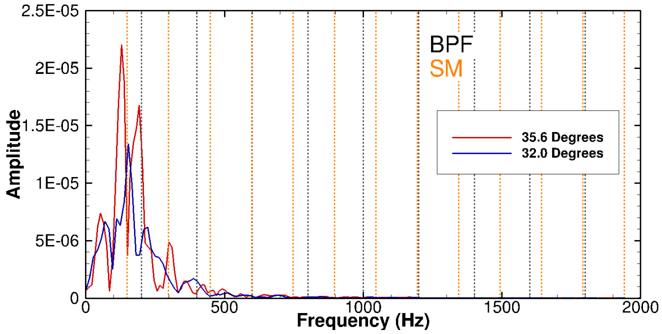

(b) Mode 1.

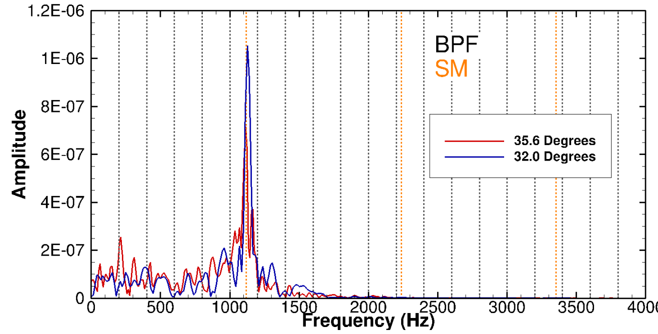

(c) Mode 4.

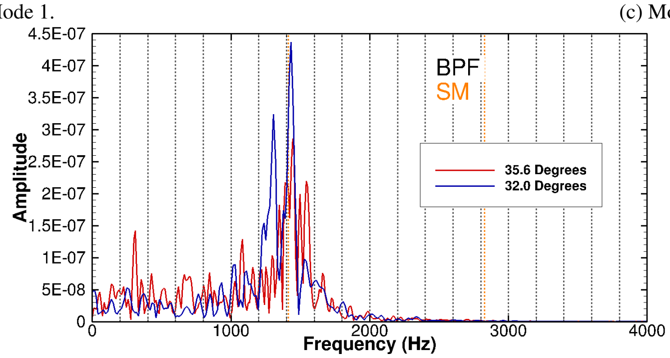

(b) Mode 5.

Figure 16. Frequency content of modal amplitudes for the MENtOR blade. Black dashed lines are the BPF and their harmonics, orange dashed lines are the eigen-modes and their harmonics, 3000 RPM, advance ratio J=0.3, pitch angles of 32 and 35.6 degrees at 75%R.

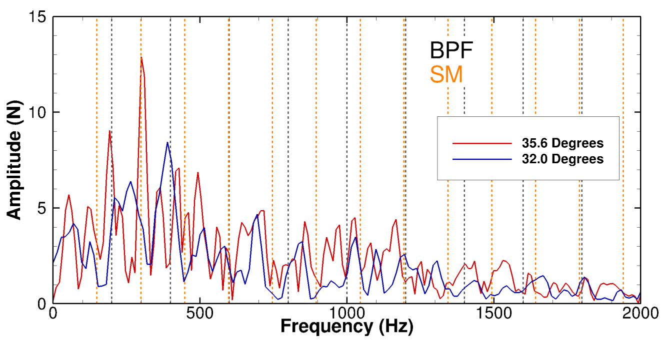

(b) Mode 1.

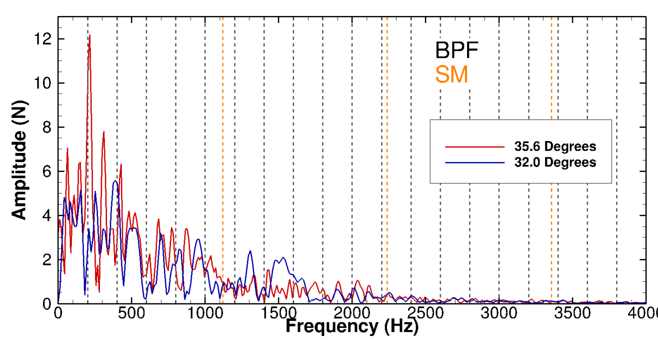

(c) Mode 4.

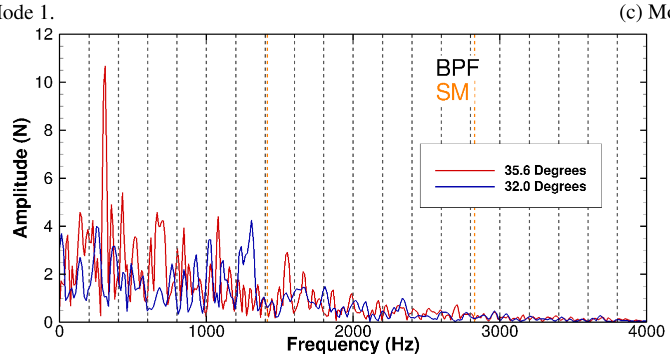

(b) Mode 5.

Figure 17. Frequency content of modal forces for the MENtOR blade. Black dashed lines are the BPF and their harmonics, orange dashed lines are the eigen-modes and their harmonics, 3000 RPM, advance ratio J=0.3, pitch angles of 32 and 35.6 degrees at 75%R.

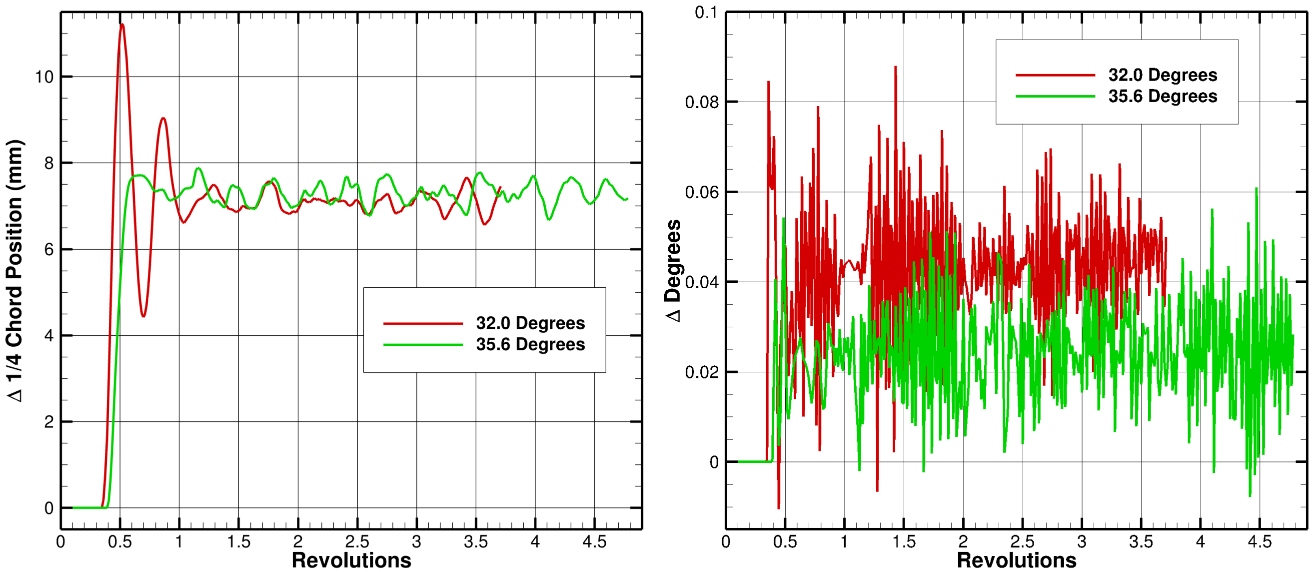

(a) Quarter chord tip displacement.

(b) Change in tip pitch angle.

Figure 18. Tip deflections and twist for the MENtOR blade, 3000 RPM, advance ratio J=0.3, pitch angles of 32 and 35.6 degrees at 75%R.